Chemistry–A European Journal
Research Article
doi.org/10.1002/chem.202402289
Chemistry Europe
European Chemical Societies Publishing
www.chemeurj.org

A CH_4-Driven Ion Cloud-Stretched Approach Enables ICP-*q*MS for Multiplex Single-Cell Analysis

Zhengxian Lv,[a] Xinli Yan,[a] Zhen Liu,[a] Shi Chen,[a] Xiaowen Yan,*[a, b] Limin Yang,[a] and Qiuquan Wang*[a]

In the last 40 years, inductively coupled plasma quadrupole (*q*) mass spectrometry (ICP-*q*MS) has been recognized as one of the best tools for the quantification of multiple elements/isotopes and even the biomolecules they labeled in a homogeneous solution sample. However, it meets a tough challenge when acquiring multi-m/z signals from an intact single-cell dispersed in a cell suspension, since the single-cell ion cloud generated in ICP presents an intermittently transient event with a duration time of hundreds of microseconds while the dwell time plus settling time of the *q* is at the similar time scale when peak-hopping between different m/z. Herein, we report CH_4 is able to stretch the single-cell ion cloud duration time to more than 7,000 μs in collision-reaction-cell (CRC), allowing multi-m/z signals acquisition by ICP-*q*MS. Quantification of single-cell's multiple phenotype protein markers can thus be achieved on ICP-(CH_4-CRC)-*q*MS, not only revealing the heterogeneity between the single cells but also enabling an unambiguous cell-classification of their subtypes. CH_4-driven ion cloud-stretched approach breaks through the long-standing bottleneck limited single-cell multiplex analysis on ICP-*q*MS, paving a path for more important applications of ICP-*q*MS in the fields related to single-cell analysis.

Introduction

Cells are the basic units of life. They are heterogeneous like different human individuals. It is vital to find out the cell's heterogeneity for understanding behaviors of the cells and their biofunctions, thus advancing classification of healthy cells and diseased cell subtypes as well as diagnosis and consequent decision of a treatment regimen. To this end, single-cell genomics has been a popular way to encode cells since DNA and/or RNA can be PCR-amplified that leverage their detection in a single-cell level.[1] Nevertheless, as we know that the messenger RNA and expressed protein are not always correlation with genes.[2] The cells' actual behaviors and functions are more directly reflected by the expressed proteins, which lead to various cell phenotypes. Recent advances in mass spectrometric techniques for protein analysis brought us closer to a more actual single-cell characterization.[3] It should be noted that, however, characterizing a single-cell via the determination of its proteins is a tough challenge because the absolute amounts of most proteins of interesting on/in a single-cell are around or even below the limit of detections (LODs) of most currently available soft-ionization mass spectrometric techniques, which is frequently applied to target high abundant biomolecules but not the low abundant and biologically meaningful proteins for single-cell characterization, not mentioning that the cells require enzymatic digestion and extraction steps before they can be analyzed.[4] Anyway, measurement of proteins of interest on/in an intact single-cell one-by-one with high sensitivity and high throughput is an ideal but challenging way for discovering the heterogeneity among the cells and thus classifying their subtypes. In order to achieve this, a hard ionization source-based inductively coupled plasma time-of-flight mass spectrometry (ICP-TOFMS), namely CyTOF, is an excellent example, as it may analyze intact single cells and realize a high-dimensional assay of over 40 parameters of the single-cell when replace fluorescent labels using exogenous cellular element-tags to label the targeted biomarkers.[5] Nevertheless, CyTOF is primarily utilized for Research Use Only (RUO) purposes considering its high price and operating costs.[6] Currently, CyTOF is not a widely accessible single-cell analysis tool in a clinical laboratory, becuase a typical In Vitro Diagnosis (IVD) multivariate assay practically employs only a few of definitively diagnostic meaningful biomarkers known by the physicians, and more realistically for reducing the financial burdensome of the patients.[7] We need a cost-effective and affordable tool.

ICP quadrupole (*q*) MS (ICP-*q*MS) is a more classical and economical hard-ionization mass spectrometric technique compared with ICP-TOFMS. ICP-*q*MS was originally designed for the determination of atomic composition of a sample.[8] In the high temperature ICP, which is formed by a flowing argon (Ar) stream through a high-frequency RF field, molecules, small particles, and even intact cells can be vaporized, atomized and ionized because the first ionization potentials of most elements in the Periodic Table are below that of Ar. This characteristic renders ICP-*q*MS one of the best tools for elements/isotopes analysis with LODs down to parts per billion (ppb) to parts per trillion (ppt).[9] Not limited to the determination of trace

---

[a] Z. Lv, X. Yan, Z. Liu, S. Chen, X. Yan, L. Yang, Q. Wang
Department of Chemistry & the MOE Key Lab of Spectrochemical Analysis and Instrumentation, College of Chemistry and Chemical Engineering, Xiamen University, Xiamen 361005, China
E-mail: xwyan@xmu.edu.cn
qqwang@xmu.edu.cn

[b] X. Yan
Innovation Laboratory for Sciences and Technologies of Energy Materials of Fujian Province (IKKEM), Xiamen 361005, China

Supporting information for this article is available on the WWW under https://doi.org/10.1002/chem.202402289

elements/isotopes themselves, ICP-*q*MS has been extented to quantify biomolecules through determination of the endogenous and/or stoichiometrically labeled exogenous elements/isotopes.[10] To the best of our knowledge, the multiplex quantification capability of ICP-*q*MS is mostly achieved for solution samples, in which the analytes are homogeneously dissolved. For the micro/nano particles and/or intact cells dispersed in a suspension, the ICP-generated ion clouds present intermittently transient events with a duration time of hundreds of microseconds, which requires a much faster signal acquisition frequency to distinguish the pulsed ion cloud profile from the dissolved background signals. This is a serious challenge even for state-of-the-art ICP-*q*MS since the *q* is a sequential scanning type mass analyzer whose dwell time and settling time are at the similar time scale as the single-cell ion cloud when peak-hopping between different m/z. Until now, only one up to two m/z signals acquisition from the transient single-particle and/or single-cell ion-cloud could be guaranteed[11] due to the insufficient duration time leaving for acquiring multi-m/z signals even though adding O_2 and/or NH_3 into collision-reaction-cell (CRC) to expand the ion-cloud before entering to *q*MS, which is not satisfactory for a comprehensive characterization of an intact single-cell. To the best of our knowledge, more than two m/z signals obtained from an intact single-cell on ICP-*q*MS has not been reported so far. To address such a long-standing yet unsolved issue, we have two conceivable solutions in mind. One is, of course, to increase the data acquisition frequency, i.e. shorten both the dwell and settling times of a conventionally available ICP-*q*MS. However, a too short dwell time results in an insignificant signal to noise ratio;[12] in the meantime, a too short settling time makes the signal unstable when performing the m/z-hopping experienced. The other is to find a more efficacious collision gas to stretch the length of ICP-generated single-cell ion-cloud, which may make the ion-cloud duration time longer enough for a quasi-simultaneous multi-m/z signals acquisition by *q*MS under adequate dwell and settling times. For this purpose, a more suitable pressurized collision gas should be introduced into CRC, an important component initially equipped on ICP-*q*MS for eliminating the spectral interferences from polyatomic ions.

Herein, we report the establishment of a CH_4-driven CRC ICP-*q*MS platform [ICP-(CH_4-CRC)-*q*MS] for intact single-cell multiplex analysis (Scheme 1). CH_4 can effectively stretch ICP-generated ion-cloud duration time of the single-cell during CRC for multi-m/z signals acquisition on a conventional ICP-*q*MS. This ICP-(CH_4-CRC)-*q*MS platform was first validated using commercially available lanthanide-containing polystyrene beads (Ln-PS, 3 μm; Ln = Ce, Eu, Ho, and Lu), and then applied to the quantification of protein biomarkers on an intact single-cell surface for subsequent classification of the phenotypes of model breast cancer cells (MDA-MB-231, SKBR-3, BT474 and MCF-7). Once the cells were labeled by Ln-tagged macrophage MS2 capsid-conjugated antibody (Ln-MS2-*ab*, Ln = Ce, Eu, Ho, and Lu) toward the corresponding cell surface biomarkers, i.e., epithelial cell adhesion molecule (EpCAM), epidermal growth factor receptor (EGFR), human epidermal growth factor receptor (HER2) and estrogen receptor α (ERα), they were manipulated to have an appropriate interval time via an oil-free microfluidic chip (OFMC) and on-line infused into ICP-(CH_4-CRC)-*q*MS for quantification. The model MDA-MB-231, SKBR-3, BT474 and MCF-7 cells can thus be unambiguously classified based on the contents of the biomarkers quantified on each single-cell. As far as we know, this is the first example realizing a four-parametric analysis of an intact single-cell on a conventional ICP-*q*MS, breaking through the long-standing bottleneck of ICP-*q*MS for a single-cell multiplex analysis.

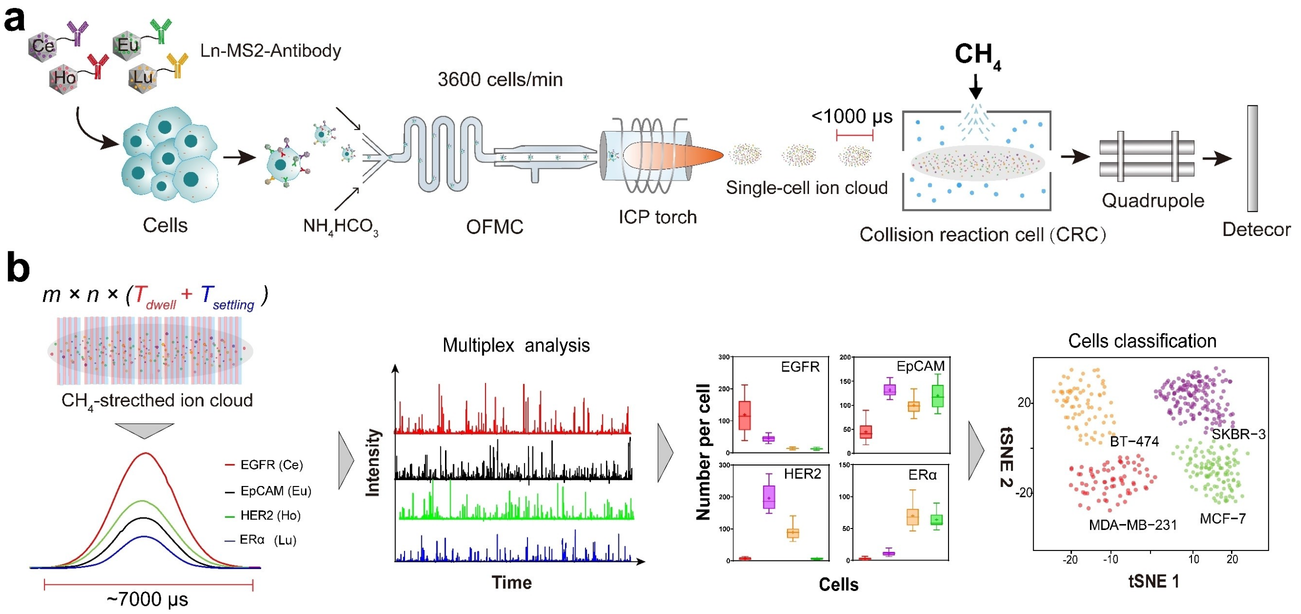

Scheme 1. Schematic diagram of the overall single-cell multiplex analysis on ICP-(CH_4-CRC)-*q*MS platform. (a) The Ln-MS2-*ab* labeled cells were lined up via OFMC and directly infused on-line into ICP, the ICP-generated single-cell ion cloud was subsequently stretched by CH_4-CRC and analyzed by ICP-*q*MS; (b) the cells were thus classified via the characteristic contents of the biomarkers on each single-cell.

Results and Discussion

Establishment of ICP-(CH_4-CRC)-*q*MS Platform

It is vital to employ appropriate dwell time (T_{dwell}) and settling time ($T_{settling}$) of ICP-*q*MS for single-cell analysis, which together set up a sweep duty cycle $T_{sweep} = T_{dwell} + T_{settlig}$ on each m/z. To achieve multi-m/z signals (*n*) acquisition of one data point from the ion-cloud of a transient single-cell event, the time needed should be equal to or greater than $n \times T_{sweep}$. Moreover, to acquire more data points (*m*) on each m/z of the multi-m/z signals (*n*), the total signal acquisition time should be equal to or greater than $m \times n \times T_{sweep}$, which should be less than the single-cell ion-cloud duration time. As previously discussed, too short T_{dwell} and $T_{settling}$ are not beneficial for obtaining a significant signal-to-noise ratio and for maintaining m/z-hopping stability. On the ICP-*q*MS instrument we used (Table S1), we selected 100 μs and 150 μs as the trade-off T_{dwell} and $T_{settling}$ (Figure S1) although they could be respectively set to as short as 10 μs and 75 μs. Subsequently, the collision gases including He, CH_4, NH_3, N_2, O_2, Ar and C_4H_{10} were investigated under different gas flowrate from 0 to 4.0 mL/min, and CRC axial field voltage (AFV) from 0 to 400 V, which can provide a supplementary electric potential within the CRC to compensate the loss of ion kinetic energy.[13] Their abilities to stretch the ion-cloud duration time were investigated using the model Ln-PS particles, as shown in Figure 1and Figure S2. Effects of the gases on ion-cloud duration presented a similar trend that increases gradually to a plateau and then descends along with the increases of the gas flowrate and AFV (Figure S2). Such observed phenomena can be ascribed to the physical collision and chemical reaction between the gas and Ln^+. Specifically, during CRC, the physical collision of NH_3 and O_2 resulted in the maximum ion signal duration times (i.e. the apparent ion-cloud duration times) of 1000 ± 50, 3500 ± 150, 3500 ± 150, 3000 ± 100, 3000 ± 100 μs for NH_3 and 750 ± 50, 1250 ± 50, 1250 ± 50, 750 ± 50, 750 ± 50 μs for O_2 when monitoring $^{140}Ce^+$, $^{151}Eu^+$, $^{153}Eu^+$, $^{165}Ho^+$, and $^{175}Lu^+$ on-mass ($n=3$); while the chemical reactions between NH_3 and/or O_2 and Ln^+[14] led to a decrease in sensitivity because of the chemical transformations of Ln^+ ions into polyatomic ions, e.g. $^{140}Ce^{15}N^1H^+$ and $^{140}Ce^{16}O^+$ (Figure S3) that were filtered out by the *q* when $^{140}Ce^+$ was monitored. Even if we could determine $^{156}[^{140}Ce^{15}N^1H]^+$ and $^{156}[^{140}Ce^{16}O]^+$ on a mass-shift mode, their sensitivities still decreased mainly due to the 'chemical dilution effect' on the total ions as a result of the incomplete chemical transformations. NH_3 and O_2 were therefore excluded, although they were the two frequently-used collision gases in the noble metal nanoparticles analysis using ICP-*q*MS.[11,15] Among the rest chemically 'inert' gases toward Ln^+, we found that CH_4 is most effective to stretch the ion-cloud with the duration time up to a maxima of 7000 ± 250 ($^{140}Ce^+$), 7250 ± 250 ($^{151}Eu^+$), 7250 ± 250 ($^{153}Eu^+$), 7100 ± 250 ($^{165}Ho^+$), and 7100 ± 250 ($^{175}Lu^+$) μs under the flowrate of 2.5 mL/min and AFV of 300 V ($n=3$) (Figure 1), followed by N_2 (2000 ± 100, 5250 ± 200, 5250 ± 200, 4500 ± 200 and 4500 ± 150 μs), C_4H_{10} (1000 ± 50, 2000 ± 50, 2000 ± 50, 1750 ± 50 and 1750 ± 50 μs), Ar (1850 ± 50, 1650 ± 50, 1650 ± 50, 1650 ± 50 and 1650 ± 50 μs), and He (1250 ± 50, 1250 ± 50, 1250 ± 50, 1250 ± 50 and 1250 ± 50 μs) under their corresponding optimized conditions.

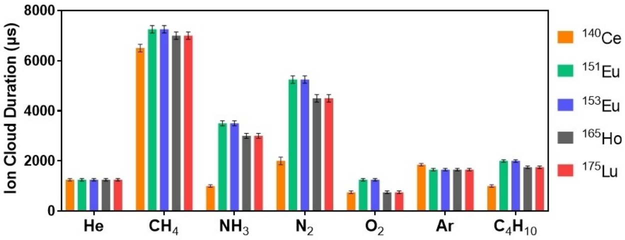

Figure 1. Duration time of the ion-cloud of Ln-PS using different collision gas and AFV: He (3.0 mL/min, AFV = 200 V); CH_4 (2.5, 300); NH_3 (0.5, 200); N_2 (2.4, 300); O_2 (0.6, 300); Ar (1.0, 200); and C_4H_{10} (0.5, 300).

Take $^{153}Eu^+$ as an example, along with the increase in CH_4 flowrate to 2.5 mL/min, the ion cloud duration time is broadening to a maximum duration time of 7250 ± 250 μs accompanying by a gradually increase in $^{153}Eu^+$ signal strength due to the reduced pulse pile-up effect;[16] this tendency continues until collision scattering energy loss starts to become dominant when the gas flowrate is higher than 2.5 mL/min (Figure 2a). On the other hand, increased AFV compensates the loss of ion kinetic energy and leads to a relative increase in signal intensity (Figure 2b). However, an excessive AFV (e.g. 400 V) may in turn hinder ion kinetic energy distribution, compressing the ion cloud duration time down to 5500 ± 250 μs (Figure 2a). Therefore, a balance must be obtained between the collision gas flowrate and AFV that significantly influence the ion cloud duration time. The representative peak profiles of $^{153}Eu^+$ automatically plotted by the Syngistix software are shown in (Figure S4).

In addition to the gas flowrate and AFV, we found that the ion-cloud duration time stretched by the collision gases is according to their molecular mass (Figure 1). These experimental results seem to be contrary to our instinctive expectation that the ion cloud duration time would be more effectively stretched by the gas of higher molecular weight, in the order of

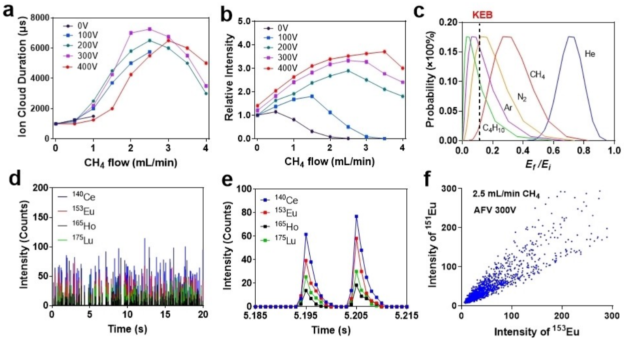

Figure 2. Impacts of CH_4 flowrate and CRC AFV on (a) the ion-cloud duration time and (b) signal intensity of $^{153}Eu^+$. (c) E_f/Ei Poisson distribution probabilities of $^{153}Eu^+$ after the ions experienced 5 times collisions ($\overline{N}=5$) during CRC when using different collision gases. (d, e) Single-particle analysis of Ln-PS in a 3.0×10^5 particle/mL suspension on ICP-(CH_4-CRC)-*q*MS. (f) Intensity correlation between $^{151}Eu^+$ and $^{153}Eu^+$.

C_4H_{10} (58 Da) > Ar (40) > N_2 (28) > CH_4 (16) > He (4), since the gases with higher molecular weights have higher collision diameter (0.54, 0.37, 0.38, 0.38, 0.21 nm) and/or cross-section (0.43, 0.25, 0.26, 0.26, 0.13 nm^2).[17] We speculate that variation in the ion kinetic energy caused by collisions is a root factor contributing to the final ion-cloud duration time. A wider ion kinetic energy distribution in CRC means more asynchronous ions of the radial velocity directed to the exit,[18] leading to a longer ion cloud duration time. When the hard-sphere collision model assuming elastic interactions[19] was aptly employed to describe the kinetic energy of ions (e.g. $^{153}Eu^+$ here), its average residue energy fraction ($\frac{E_f}{E_i} = \left[\frac{m_i^2+m_g^2}{(m_i+m_g)^2}\right]^{\overline{N}}$, where $\overline{N}$ is the collision number; E_i and E_f represent kinetic energy of the ion before and after collision; and m_i and m_g the molecular weight of the ion and gas.) were calculated to be 0.950 (He), 0.829 (CH_4), 0.738 (N_2), 0.671 (Ar), and 0.601 (C_4H_{10}) after one collision ($\overline{N}=1$). We may imagine that the more collisions the ions undergo during CRC, the more energy the ions lose. This might lead to such a consequence that the ions with a beyond *q* kinetic energy barrier (KEB) would be excluded by the *q* mass filter even though their m/z does not change. If we set KEB as $E_f/E_i = 10\%$ and assume the ions experience 5 times collisions ($\overline{N}=5$) during CRC, the Poisson distribution probabilities of $^{153}Eu^+$ lower than KEB were calculated to be 0% (He), 0.5% (CH_4), 23.8% (N_2), 56% (Ar) and 73.5% (C_4H_{10}) according to $P(E_f/E_i) = \frac{(\overline{N})^{E_f/E_i}}{E_f/E_i!} e^{-\overline{N}}$ (Figure 2c). These results suggested that a heavier gas is more efficient in damping the ion kinetic energy, resulting in a higher proportion of the ions lower than KEB; while a lighter may facilitate the retention of a larger percentage of initial ion energy. Larger proportion (73.5%) of the ions lower than KEB in the case of C_4H_{10} implies a lower *q* passrate (26.5%). This should be responsible to the narrower ion-cloud duration time determined by *q*MS when using C_4H_{10}. While CH_4 is best with the widest ion-cloud duration observed among the gases investigated owing to the 95% *q* passrate of $^{153}Eu^+$ and its suitable average residue energy fraction ($E_f/E_i = 0.829$). Besides, it is worth noting that polarizability (α) of the collision gas might be another factor responsible for C_4H_{10} and CH_4, for example, regarding their ion-cloud stretching outcomes. Easier polarizable C_4H_{10} ($\alpha = 8.01\times10^{-40}$ cm^2/V) than CH_4 ($\alpha = 3.00\times10^{-40}$ cm^2/V)[20] leads to a more significant loss of ion kinetic energy in the form of internal energy[21] as more inelastic collisions happened between Ln^+ and C_4H_{10}. It should be also noted that He should be a good collision gas for CRC to eliminate the spectral interferences (*q* passrate 100%) but not good for stretching the ion-cloud duration time because of its very weak ability for diversifying the ion kinetic energy ($E_f/E_i = 0.950$).

Afterwards, we analyzed a suspension sample of 3.0×10^5 Ln-PS/mL on ICP-(CH_4-CRC)-*q*MS monitoring $^{140}Ce^+$, $^{153}Eu^+$/$^{151}Eu^+$, $^{165}Ho^+$ and $^{175}Lu^+$. 1194±25 positive four-m/z events out of theoretical 1,200 Ln-PS beads within 20 s were detected (n=7) with a recovery of 99.5% (Figure 2d) using 2.5 mL/min CH_4 and 300 V CRC AFV under the assistance of OFMC.[22] The interval time between the adjacent individual Ln-PS beads could be adjusted by OFMC to more than 8,000 μs when the Ln-PS suspension flowrate was set at 12 μL/min and the supplementary NH_4HCO_3 flowrate 10 μL/min (Figure S5). Considering that 100 μs dwell time and 150 μs settling time were employed, one sweep duty cycle time on each m/z was 250 μs. For the four-m/z mode, the total integration time for each m/z data point was 1000 μs (4×250), this means that 7 data points required on each m/z from the more than CH_4-stretched 7,000 μs ion-cloud duration was achieved (Figure 2e). Such a long ion-cloud duration time achieved enables a quasi-simultaneous multi-m/z signals acquisition for a more representative single-particle profiling. Further extracting the intensity data of $^{151}Eu^+$ and $^{153}Eu^+$ from the individual beads, a Pearson correlation coefficient of 0.932 between their intensities was found (Figure 2f). The ratio of $^{151}Eu^+$ to $^{153}Eu^+$ was measured to be 0.883±0.027 (n=7) with an acceptable negative error of −3.3% compared to 0.916 of their natural abundance (^{151}Eu 47.81% and ^{153}Eu 52.19%). Moreover, we measured Gd isotope abundance of ^{156}Gd, ^{157}Gd, ^{158}Gd, and ^{160}Gd in the Gd-PS beads (Figure S6). The obtained results indicated that the abundance of ^{156}Gd, ^{157}Gd, ^{158}Gd, and ^{160}Gd are (20.84±1.3)% (n=7) with 1.8% relative error corresponding to the natural abundance value of 20.47%, (15.42±0.7)% (−1.5% to 15.65%), (24.98±1.4)% (0.6% to 24.84%), and (21.58±0.9)% (−1.3% to 21.96%), respectively. These outcomes suggested that ICP-(CH_4-CRC)-*q*MS works well, validating its feasibility of a four-m/z analysis.

Based on the corresponding dissolved standard mass flux calibration curves (Figure S7),[23] the Ce, Eu, Ho, and Lu contents in Ln-PS were then determined. The Ln absolute contents in Ln-PS determined under both single-m/z and four-m/z modes are listed in Table 1. The mass limit of detection (LOD_{mass}) was estimated based on the commonly adopted 3σ criterion, implying that more than 90% decrease in sensitivity under the four-m/z mode relative to the single-m/z mode. Such a decrease in sensitivity is ascribed to the decrease of ion density in the CH_4-stretched ion-cloud and the existence of vacant settling time (150 μs) as well when m/z-hopping. Based on LOD_{mass} obtained under the four-m/z mode, the element number LOD (LOD_{atom}) were calculated to be 38.1×10^4 (Ce), 28.2×10^4 (Eu), 34.4×10^4 (Ho) and 33.7×10^4 (Lu) atoms per Ln-PS. Considering LOD_{atom} is corresponding to the lowest detectable number of the biomarkers on each cell when they were quantitatively labeled with Ln-tag, the lower abundant biomarkers[24] expressed on single-cell surface would hardly be quantified. This should be another issue hampering ICP-*q*MS for single-cell multiplex analysis, which should be overcome before the performance of single-cell multiplex analysis on the established ICP-(CH_4-CRC)-*q*MS platform.

Single-cell Multiplex Analysis on ICP-(CH_4-CRC)-*q*MS Platform

Fortunately, the viruslike Ln-MS2 signal-amplifier[25] developed previously in our lab, which could carry hundreds of Ln atoms on each MS2 capsid, may compensate the sensitivity loss. We respectively conjugated Ln-MS2 (Ln=Ce, Eu, Ho, and Lu) to the antibodies of EGFR, EpCAM, HER2 and ERα via maleimide-thiol

Table 1. The mean intensity and mass of Ce, Eu, Ho and Lu per Ln-PS, *LOD*$_{mass}$ and *LOD*$_{atom}$ under both single-m/z (*S*) and four-m/z (*F*) measurement modes (n = 7), and the corresponding sensitivity decrease.

		Mean intensity counts/RSD%	Mass (ag)	Relative error[a]	LOD		Decrease in sensitivity
					Mass (ag)	Atom ×10	
^{140}Ce	*S*	1271.9/3.6	986.0 ± 34.2	9.8 %	6.5	2.8	92.6 %
	F	84.4/7.2	889.1 ± 69.8		88.6	38.1	
^{153}Eu	*S*	1039.1/4.3	753.2 ± 42.5	8.7 %	6.1	2.4	91.5 %
	F	80.8/7.7	687.5 ± 73.2		71.8	28.2	
^{165}Ho	*S*	747.2/3.7	546.1 ± 38.4	9.9 %	6.2	2.4	93.4 %
	F	43.7/6.5	491.3 ± 66.4		94.3	34.4	
^{175}Lu	*S*	989.9/4.4	723.7 ± 43.7	8.3 %	6.4	2.2	93.5 %
	F	57.5/7.3	671.8 ± 78.8		97.9	33.7	

[a] Relative error was calculated based on the absolute amount of elements quantified under the four-m/z mode relative to the values obtained under the single-m/z mode.

reaction to obtain *anti*EGFR-MS2-Ce$_{973}$, *anti*EpCAM-MS2-Eu$_{973}$, *anti*HER2-MS2-Ho$_{973}$, and *anti*ERα-MS2-Lu$_{973}$ tags (See the details in the Supporting Information, Figures S8–S11). These Ln-MS2-*ab* enables nearly three orders of magnitude signal-amplification after they were labeled toward the corresponding antigen molecules, compared with the corresponding antibody-DOTA-Ln containing only 8 Ln atoms (Figures S12). For example, *anti*HER2-MS2-Ho$_{973}$-labeled SKBR-3 cells were unambiguously detected compared with the *anti*HER2-(DOTA-Ho)$_8$-labeled ones in a 0.5×10^5 cells/mL suspension (Figure 3a). With the assistance of OFMC, 3,504 ± 51 single-cell events were determined out of 3,600 cells within one minute (n = 7, recovery 97.3 %) in a 3.0×10^5 cells/mL *anti*HER2-MS2-Ho$_{973}$-labeled SKBR-3 suspension (Figure 3b). Moreover, the average signal intensity of 470 ± 56 counts/cell (n = 7) determined was well comparable to 486 ± 63 counts/cell when the lower concentration cell-suspension sample of 0.5×10^5 cells/mL was used (Figure 3c), confirming that the signals acquired are exactly from the single cells with a much-improved throughput of nearly six times.

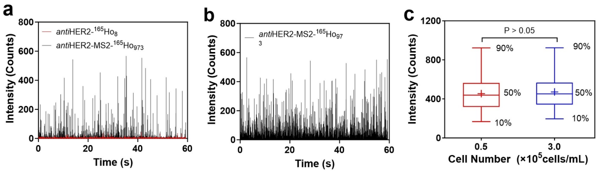

Figure 3. (a) Comparison of the signals of SKBR-3 single cells labeled by *anti*HER2-MS2-Ho$_{973}$ and *anti*HER2-(DOTA-Ho)$_8$ in 0.5×10^5 cells/mL suspension. (b) Single-cell signals from a 3.0×10^5 cells/mL suspension of the *anti*HER2-MS2-Ho$_{973}$-labeled SKBR-3 cells under the assistance of OFMC with 12 μL/min sampling flowrate and 10 μL/min supplementary NH_4HCO_3 flowrate. (c) Box plot of the $^{165}Ho^+$ intensities obtained from 0.5×10^5 cells/mL and 3.0×10^5 cells/mL of *anti*HER2-MS2-Ho$_{973}$-labeled SKBR-3 suspensions; + in the center of the boxes represents the mean value. P-value was calculated by ANOVA test (n = 7).

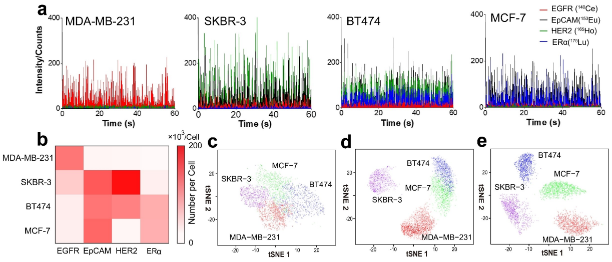

Figure 4. (a) Four-plex single-cell analysis of MDA-MB-231, SKBR-3, BT-474 and MCF-7 on ICP-(CH_4-CRC)-*q*MS platform and (b) heatmap of the average contents of EGFR, EpCAM, HER2 and ERα quantified on the single cells derived from (a). t-SNE visual classification of breast cell lines (red dots: MDA-MB-231; purple dots: SKBR-3; blue dots: BT474; and green dots: MCF-7) via (c) the dual-marker of EGFR and EpCAM, (d) the triple-marker EGFR, EpCAM and ERα, and (e) the quad-marker EGFR, EpCAM, HER2 and ERα.

We then quantified the number of EGFR, EpCAM, HER2 and ERα expressed on the surface of single cells (Figure 4a) on the optimized ICP-(CH_4-CRC)-*q*MS platform. Cells in the suspension of 1.0×10^6 cells/mL were encoded with 8 μg/mL of *anti*EGFR-MS2-Ce$_{973}$, *anti*EpCAM-MS2-Eu$_{973}$, *anti*HER2-MS2-Ho$_{973}$, and *anti*-ERα-MS2-Lu$_{973}$ for 30 minutes at 4 °C, and then diluted to 3.0×10^5 cells/mL for ICP-(CH_4-CRC)-*q*MS analysis. As shown in Figure 4b (Figure S13 and Table S2), the highly aggressive triple-negative cell line MDA-MB-231 exhibited a high content of EGFR (106.8 ± 13.5)×10^3/cell, while relatively low contents of EpCAM (7.7 ± 1.8)×10^3/cell, HER2 (6.4 ± 1.5)×10^3/cell and ERα (4.2 ± 0.6)×10^3/cell (n = 7). More importantly, MDA-MB-231 cells also exhibited the highest heterogeneity in EGFR expression with approximately 2.4-fold difference in the interquartile ranging from (65.4 ± 8.1)×10^3/cell (25 %) to (153.2 ± 17.4)×10^3/cell (75 %) (Figure S13). Such a result might be attributed to the fact that MDA-MB-231 cells are more proliferative and genome unstable in tumor, indicating an association between EGFR levels and poor breast cancer prognosis.[26] By comparison, the less aggressive luminal B BT474 cells displayed lower EGFR (14.8 ± 2.1)×10^3/cell, while higher EpCAM (107.5 ± 17.8)×10^3, HER2 (98.6 ± 13.1)×10^3, and ERα (63.4 ± 9.6)×10^3 on per cell (Figure 4b and Table S2). HER2-rich SKBR-3 cells expressed higher HER2 (187.3 ± 18.7)×10^3/cell as expected, which is approximately 30 times higher than HER2-low-expressed luminal A MCF-7 cell with (6.5 ± 0.8)×10^3 HER2/cell; while MCF-7 expressed both significant EpCAM of (118.8 ± 9.1)×10^3/cell and ERα (62.1 ± 5.5)×10^3/cell similar to those of BT474 ($p > 0.05$) (Figure S13), indicating a higher degree of prototype similarity between luminal A MCF-7 and luminal B BT474 subtypes.[27] These obtained results demonstrated the corresponding phenotype biomarkers vary across different cell lines at single-cell level, being beneficial for subsequent cell classification.

Finally, we mapped the quantitative data sets of the single cells analyzed by ICP-(CH_4-CRC)-*q*MS onto a two-dimensional plane in an unbiased fashion using t-distributed Stochastic Neighbor Embedding (t-SNE) for classification of the cells. An unsupervised classification of four clusters was observed as shown in Figure 4c for dual-marker (EGFR and EpCAM), Figure 4d triple-marker (EGFR, EpCAM and ERα) and Figure 4e quad-marker (EGFR, EpCAM, HER2 and ERα) at a perplexity value of 50, in which each point represents a single cell. These results shown in the t-SNE figures evidenced that the quad-marker is much more distinguishable for classifying cell lines of MDA-MB-231, SKBR-3, BT-474 and MCF-7 compared to the dual-marker and triple-marker, highlighting the importance of higher multiplex single-cell analysis achieved on ICP-(CH_4-CRC)-*q*MS platform.

Conclusions

We developed an ICP-(CH_4-CRC)-*q*MS platform, realizing the long-pending expectation of single-cell multiplex analysis on a conventional ICP-*q*MS. On this established platform, the ion-cloud duration time of a single-cell event could be stretched over 7,000 μs by pressurizing CH_4 into CRC, allowing *q*MS to acquire four-m/z signals from a single cell. Simultaneous quantification of EGFR, EpCAM, HER2 and ERα expressed on the surface of intact single cells achieved an unambiguous classification of MDA-MB-231, SKBR-3, BT-474 and MCF-7 breast cancer cell lines. This four-plex single-cell analysis on a conventional ICP-*q*MS sets an example for applying ICP-*q*MS to a practical IVD multivariate assay, during which, considering a least burdensome on patients,[7] only several critical disease-decisive phenotype biomarkers are determined for physicians to make a reasonable treatment decision. Compared with the expensive CyTOF,[5,6] CH_4-stretched single-cell ion-cloud strategy will make ICP-*q*MS a more cost-effective tool for not only basic biological research but also routine clinical IVD applications. Last but not the least, we might also expect more m/z signals acquisition from a single-cell would be possible if a more effective collision gas could be found as more in-depth research undergoes, and a shorter $T_{settling}$ could be reached as the continuous advancement of ICP-*q*MS instrumentation, as well as a greater stoichiometric signal-amplification element/isotope tag could be designed and fabricated in the near future.

Supporting Information Summary

The authors have cited additional references within the Supporting Information;[21,23,25] Materials and Instrumentation; Preparation of Ln-MS2-*ab*; Cell Culturing and Labeling; Data Processing; Figure S1–13; Table S1–2.

Acknowledgements

This study was financially supported by the National Natural Science Foundation of China (Grant No. 22193053, 21535007, and 22074127) and the National Key Research and Development Program of China (2022YFF0710200). The authors declare no competing financial interests.

Conflict of Interests

The authors declare no conflict of interest.

Data Availability Statement

The data that support the findings of this study are available from the corresponding author upon reasonable request.

Keywords: ICP-*q*MS · Single-Cell Multiplex Analysis · CH_4 · Collision-Reaction-Cell · Breast Cancer Cells

[1] R. Elmentaite, C. D. Conde, L. Yang, S. A. Teichmann, *Nat. Rev. Genet.* **2022**, *23*, 395–410.

[2] a) Y. Liu, A. Beyer, R. Aebersold, *Cell* **2016**, *165*, 535–550; b) C. Buccitelli, M. Selbach, *Nat. Rev. Genet.* **2020**, *21*, 630–644.

[3] a) H. M. Bennett, W. Stephenson, C. M. Rose, S. Darmanis, *Nat. Methods.* **2023**, *20*, 363–374; b) Y. R. Jiang, L. Zhu, L. R. Cao, Q. Wu, J. B. Chen, Y. Wang, J. Wu, T. Y. Zhang, Z. L. Wang, Z. Y. Guan, Q. Q. Xu, Q. X. Fan, S. W. Shi, H. F. Wang, J. Z. Pan, X. D. Fu, Y. Wang, Q. Fang, *Cell Rep.* **2023**, *42*, 113455.

[4] a) N. Slavov, *Curr. Opin. Chem. Biol.* **2021**, *60*, 1–9; b) H. Yao, H. Zhao, X. Zhao, X. Pan, J. Feng, F. Xu, S. C. Zhang, X. R. Zhang, *Anal. Chem.* **2019**, *91*, 9777–9783; c) P. Zhao, Y. Feng, J. Wu, J. Zhu, J. Yang, X. Ma, Z. Ouyang, X. R. Zhang, W. Zhang, W. Wang, *Anal. Chem.* **2023**, *95*, 7212–7219.

[5] a) D. R. Bandura, V. I. Baranov, O. I. Ornatsky, A. Antonov, R. Kinach, X. Lou, S. Pavlov, S. Vorobiev, J. E. Dick, S. D. Tanner, *Anal. Chem.* **2009**, *81*, 6813–6822; b) S. C. Bendall, E. F. Simonds, P. Qiu, E. D. Amir, P. O. Krutzik, R. Finck, R. V. Bruggner, R. Melamed, A. Trejo, O. I. Ornatsky, R. S. Balderas, S. K. Plevritis, K. Sach, D. Pe'er, S. D. Tanner, G. P. Nolan, *Science.* **2011**, *332*, 687–696; c) M. H. Spitzer, G. P. Nolan, *Cell.* **2016**, *165*, 780–791; d) G. Han, M. H. Spitzer, S. C. Bendall, W. J. Fantl, G. P. Nolan, *Nat. Protoc.* **2018**, *13*, 2121–2148.

[6] A. Iyer, A. A. Hamers, A. B. Pillai, *Front. Immunol.* **2022**, *13*, 815828.

[7] a) Z. Zhang, D. W. Chan, *Cancer Epidemiol. Biomarkers Prev.* **2010**, *19*, 2995–2999; b) U.S FDA. The Least Burdensome Provisions Concept and Principles. FDA-2017-D-6702, **2019**.

[8] R. S. Houk, V. A. Fassel, G. D. Flesch, H. J. Svec, A. L. Gary, C. E. Taylor, *Anal. Chem.* **1980**, *52*, 2283–2289.

[9] a) R. S. Houk, *Anal. Chem.* **1986**, *58*, 97A–105A; b) T. Van Acker, S. Theiner, E. Bolea-Fernandez, F. Vanhaecke, G. Koellensperger, *Nat. Rev. Methods Primers.* **2023**, *3*, 1–18.

[10] a) A. Sanz-Medel, M. Montes-Bayon, M. D. R. F. De La Campa, J. R. Encinar, J. Bettmer, *Anal. Bioanal. Chem.* **2008**, *390*, 3–16; b) X. W. Yan, L. M. Yang, Q. Q. Wang, *Anal. Bioanal. Chem.* **2013**, *405*, 5663–5670; c) S. D. Tanner, V. I. Baranov, O. I. Ornatsky, D. R. Bandura, T. C. George, *Cancer Immunol. Immunother.* **2013**, *62*, 955–965; d) R. Liu, S. Zhang, C. Wei, Z. Xing, S. C. Zhang, X. R. Zhang, *Acc. Chem. Res.* **2016**, *49*, 775–783; e) M. Resano, M. Aramendia, E. Garcia-Ruiz, A. Bazo, E. Bolea-Fernandez, F. Vanhaecke, *Chem. Sci.* **2022**, *13*, 4436–4473; f) L. P. Arnett, R. Rana, W. W. Y. Chung, X. C. Li, M. Abtahi, D. Majonis, J. Bassan, M. Nitz, M. A. Winnik, *Chem. Rev.* **2023**, *123*, 1166–1205.

[11] a) E. Bolea-Fernandez, D. Leite, A. Rua-Ibarz, T. Liu, G. Woods, M. Aramendia, M. Resano, F. Vanhaecke, *Anal. Chim. Acta.* **2019**, *1077*, 95–106; b) K. H. Chun, J. T. S. Lum, K. S. Y. Leung, *Anal. Chim. Acta.* **2022**, *1192*, 339389; c) X. W. Tian, H. W. Jiang, M. Wang, W. B. Cui, Y. Y. Guo,

L. N. Zheng, L. G. Hu, G. B. Qu, Y. G. Yin, Y. Cai, G. B. Jiang, *Anal. Chim. Acta.* **2023**, *1240*, 340756.

[12] A. Kana, M. Loula, R. Koplik, M. Vosmanska, O. Mestek, *Talanta.* **2019**, *197*, 189–198.

[13] D. R. Bandura, V. I. Baranov, S. D. Tanner, *J. Am. Soc. Mass Spectrom.* **2002**, *13*, 1176–1185.

[14] a) G. K. Koyanagi, P. Cheng, D. K. Bohme, *J. Phys. Chem. A* **2010**, *114*, 241–246; b) G. K. Koyanagi, D. K. Bohme, *J. Phys. Chem. A* **2001**, *105*, 8964–8968.

[15] a) N. D. Donahue, V. Sheth, A. N. Frickenstein, A. Holden, S. Kanapilly, C. Stephan, S. Wilhelm, *Nano Lett.* **2022**, *22*, 4192–4199; b) N. D. Donahue, S. Kanapilly, C. Stephan, M. C. Marlin, E. R. Francek, M. Haddad, J. Guthridge, S. Wilhelm, *Nano Lett.* **2021**, *22*, 294–301.

[16] L. A. Rush, M. C. Endres, M. Liezers, J. D. Ward, G. C. Eiden, A. M. Duffin, *Talanta.* **2018**, *189*, 268–273.

[17] B. I. Loukhovitski, A. S. Sharipov, *J. Phys. Chem. A* **2021**, *125*, 5117–5123.

[18] D. R. Bandura, V. I. Baranov, S. D. Tanner, *J. Anal. At. Spectrom.* **2000**, *15*, 921–928.

[19] N. Yamada, *Spectrochim. Acta Part B* **2015**, *110*, 31–44.

[20] H. H. Cornehl, C. Heinemann, D. Schroeder, H. Schwarz, *Organometallics.* **1995**, *14*, 992–999.

[21] K. Harouaka, C. Allen, E. Bylaska, *Spectrochim. Acta Part B* **2021**, *186*, 106309.

[22] Y. Zhou, Z. Chen, J. Zeng, J. Zhang, D. Yu, B. Zhang, X. W. Yan, L. M. Yang, Q. Q. Wang, *Anal. Chem.* **2020**, *92*, 5286–5293.

[23] H. E. Pace, N. J. Rogers, C. Jarolimek, V. A. Coleman, C. P. Higgins, J. F. Ranville, *Anal. Chem.* **2011**, *83*, 9361–9369.

[24] J. P. da Costa, P. S. M. Santos, R. Vitorino, T. Rocha-Santos, A. C. Duarte, *TrAC Trends Anal. Chem.* **2017**, *93*, 171–182.

[25] a) R. Yuan, F. Ge, Y. Liang, Y. Zhou, L. M. Yang, Q. Q. Wang, *Anal. Chem.* **2019**, *91*, 4948–4952; b) Z. Liu, Y. Liang, Y. Zhou, F. Ge, X. W. Yan, L. M. Yang, Q. Q. Wang, *iScience* **2021**, *24*, 102397.

[26] P. Bouchal, O. T. Schubert, J. Faktor, L. Capkova, H. Imrichova, K. Zoufalova, V. Paralova, R. Hrstka, Y. Liu, H. A. Ebhardt, E. Budinska, R. Nenutil, R. Aebersold, *Cell Rep.* **2019**, *28*, 832–843.

[27] C. Zhang, W. Sheng, M. Al-Rawe, T. M. Mohiuddin, M. Niebert, F. Zeppernick, I. Meihold-Heerlein, A. F. Hussain, *Int. J. Mo. Sci.* **2022**, *23*, 6122.

Manuscript received: August 12, 2024
Accepted manuscript online: October 24, 2024
Version of record online: ■■, ■■

RESEARCH ARTICLE

Z. Lv, X. Yan, Z. Liu, S. Chen, X. Yan, L. Yang, Q. Wang**

1 – 8

A CH_4-Driven Ion Cloud-Stretched Approach Enables ICP-*q*MS for Multiplex Single-Cell Analysis

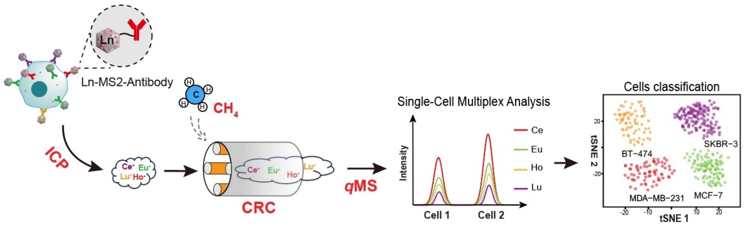

Inductively coupled plasma quadrupole mass spectrometry (ICP-*q*MS) is now able to perform a multiplex single-cell analysis based on a CH_4-driven CRC-stretched ion cloud approach. A CH_4-driven collision-reaction-cell (CRC)-stretched ion cloud approach (CH_4-CRC) enables inductively coupled plasma quadrupole mass spectrometry (ICP-*q*MS) to perform a multiplex single-cell analysis. Quantification of single-cell's multiple phenotype protein markers can thus be achieved on ICP-(CH_4-CRC)-*q*MS, not only revealing the heterogeneity between the single cells but also realizing an unambiguous cell-classification of their subtypes.